FISFVIFR

Contents lists available at ScienceDirect

Mechanical Systems and Signal Processing

journal homepage: www.elsevier.com/locate/ymssp





Damage identification for beam-like structures based on proper orthogonal modes of guided wavefields

Wei Zhou, Y.F. Xu*

Department of Mechanical and Materials Engineering, University of Cincinnati, Cincinnati, OH 45221, USA

ARTICLE INFO

Communicated by W. Ostachowicz

Keywords:
Damage identification
Proper orthogonal decomposition
Proper orthogonal modes
Continuous wavelet transform
Vanishing moments

ABSTRACT

Damage in structures can cause local anomalies in a guided wavefield due to reflection of guided waves in neighborhoods of damage. These local anomalies can be used for baseline-free damage identification if the structures are geometrically smooth and made of materials that have no stiffness and mass discontinuities. Recently, guided wavefield-based methods have been studied for damage identification by extracting and localizing local anomalies in guided wavefields in the time- and frequency-wavenumber domains. Meanwhile, proper orthogonal modes (POMs) obtained by the proper orthogonal decomposition have been studied for vibration-based damage identification. In this paper, the effectiveness of POMs of guided wavefields for damage identification in beam-like structures is studied. Since local anomalies in the POMs can be covered by global trends of the POMs, the continuous wavelet transform is used to suppress the global trends and intensify the local anomalies. The fundamental mechanism of how the continuous wavelet transform with Gaussian wavelet functions of a proper order can suppress the global trends of POMs and intensify local anomalies of POMs is explained. Significant POMs used for damage identification are determined by an adaptive truncation technique. The proper orders of the Gaussian wavelet functions, i.e., their number of vanishing moments, are determined based on the modal assurance criterion and a statistical criterion. The continuous wavelet transform of the significant POMs with Gaussian wavelet functions of the proper orders is used to yield an accumulative damage index. Numerical and experimental investigations of the proposed method are conducted on damaged beam-like structures. Their results verified that the proposed method is accurate and noise-robust for identifying the location and extent of damage in beam-like structures.

1. Introduction

Engineering structures in service bear operational loads and long-term environmental effects, which cause unwanted structural failures and casualties. The necessities of lowering the possibility of failures and extending the useful lives of the structures motivate to develop accurate and noise-robust damage identification methods, which can lead to efficient early maintenance operations. Recently, guided wavefield-based methods for damage identification have been studied widely thanks to the availability of scanning laser Doppler vibrometers (SLDVs), which can measure vibrational velocities of points on a predefined grid assigned to a structure. Reconstructing time-domain SLDV measurements allows the visualization and post-processing of a guided wavefield [1]. A guided wavefield can show features of guided waves propagating along a structure and their interactions with discontinuities associated

E-mail addresses: zhouw6@mail.uc.edu (W. Zhou), xu2yf@uc.edu (Y.F. Xu).

^{*} Corresponding author.

with damage. The interactions can be referred to as local anomalies, which can be intensified to identify the location and extent of the damage by advanced signal processing techniques [2].

The use of guided wavefields measured by an SLDV for damage identification was first introduced in Ref. [3], where the maximum amplitudes of guided waves were used for damage identification. To further exploit a guided wavefield, root mean square values of the time-history of each measurement point on an assigned grid measured by an SLDV were used for damage identification [2]. However, incident waves generated at excitation points can cause a large interference for damage identification. A trend removal algorithm based on the location of a source transducer was then developed to alleviate the adverse effects of such interference [4]. Besides, an energy-based time window was used in Refs. [5,6], where guided waves were not used in the period of excitation to alleviate the adverse effects of such interference. These two techniques are removing incident waves in the time-domain, but the interaction between incident waves and reflected waves cannot be considered. Incident waves can be isolated from propagating waves in the frequency wavenumber-domain, as reflections caused by the existence of damage are propagating in opposite directions to that of incident waves in this domain [7]. A frequency wavenumber filtering was proposed for removing incident waves and improving visualization in guided wavefield-based methods [1]. Further, two techniques, a two-dimensional Fourier transform deployed in polar coordinates and a three-dimensional Fourier transform deployed in Cartesian coordinates, were studied as frequency wavenumber filtering [8]. Local wavenumber techniques were introduced, where the size and depth of damage were quantified by matching wavenumber estimates to theoretical dispersion curves in Refs. [9,10]. Besides, a short-space frequency wavenumber technique was introduced simultaneously, which yielded a frequency wavenumber spectrum at various spatial locations for damage identification [11].

Proper orthogonal decomposition (POD) is a multi-variate statistical method that aims at obtaining an approximate representation of high-dimensional data [12]. The approximate representation is achieved by extracting proper orthogonal modes (POMs) and Galerkin projecting the POMs into a lower-dimensional model [13]. The POMs is a set of optimal orthogonal modes of analyzed data and they can capture features of the data. The effectiveness of damage identification based on POMs has been widely studied in vibration-based methods [13–17]. The difference between POMs at damaged and pristine states of a structure was exploited for a damage index in Refs. [14,15]. In Ref. [13], a POMs-based method was developed for damage identification: POMs were used to filter out the changes corresponding to different loading conditions on a structure and reserve only those caused by damage [13]. Baseline data of a pristine state of a structure are required in Refs. [13–15], which is, however, difficult to obtain in practice. Baseline-free damage identification methods have been explored based on POMs. POM energy curvature obtained from the frequency response function data was used to develop a damage index in Ref. [16]. Besides, mode shape curvature of the first POM denoised by continuous wavelet transform (CWT) was used for damage identification in connections of steel moment resisting frames [17]. To date, the two categories of damage identification methods, i.e., the ones based on guided wavefields and those based on POMs of vibrational responses, are separately studied and the effectiveness of their combination has not been investigated.

To study the effectiveness of damage identification by POMs of guided wavefields, a baseline-free and noise-robust damage identification method is proposed for beam-like structures in this paper. It identifies the location and extent of damage based on POMs of guided wavefields. The novel damage identification technique is introduced by combining the POD and the CWT. The fundamental mechanism of how the CWT can suppress the global trends of the POMs and intensify local anomalies of the POMs is investigated and explained. An adaptive truncation technique based on an empirical threshold is developed to determine significant POMs for damage identification. The modal assurance criterion and a statistical criterion are used to determine the proper orders of Gaussian wavelet functions, i.e., their number of vanishing moments. The CWT of the significant POMs with the proper orders of Gaussian wavelet functions is used to yield an accumulative damage index. The accuracy and noise-robustness of the proposed method are investigated in a numerical example of a damaged beam-like structure with different noise levels and guided wavefields with different excitation scenarios. An experimental investigation was conducted on a damaged aluminum beam-like structure undergoing different excitation scenarios.

The rest of the paper is arranged as follows. In Section 2, the proposed damage identification method based on POMs of guided wavefields is presented. In Sections 3 and 4, the numerical and experimental investigations are described, respectively. Conclusions of this work are presented in Section 5.

2. Methodology

In this section, the formulation of POD for a guided wavefield of a beam-like structure is provided, based on which the singular value decomposition (SVD) is shown. The mechanism of CWT for suppressing global trends of POMs and isolating their local anomalies is studied. The proposed damage identification method is described with: (1) truncation for significant POMs, (2) determination of the proper order of Gaussian wavelet functions for the CWT, and (3) formulation of the accumulative damage index.

2.1. POMs of guided wavefields

Let w(x,t) be a zero-mean spatial-temporal guided wavefield of a beam-like structure, in which $x \in [0,L]$ and $t \in [0,T]$ denote the space and time, respectively, with L and T being the spatial and temporal lengths of w(x,t), respectively. The POD is capable of decomposing w(x,t) as [18]

$$w(x,t) = \sum_{i=1}^{\infty} \phi_i(x) a_i(t)$$
(1)

where $a_i(t)$ and $\phi_i(x)$ are the *i*th time- and spatial-functions, respectively, and $\phi_i(x)$ is often referred to as the *i*th POM of w(x,t). Let **A** be the matrix containing w(x,t) that is uniformly sampled in a spatially, temporally uniform manner:

$$\mathbf{A} = \begin{bmatrix} w(x_1, t_1) & w(x_1, t_2) & \cdots & w(x_1, t_N) \\ w(x_2, t_1) & w(x_2, t_2) & \cdots & w(x_2, t_N) \\ \vdots & \vdots & \ddots & \vdots \\ w(x_M, t_1) & w(x_M, t_2) & \cdots & w(x_M, t_N) \end{bmatrix}$$
(2)

where $x_1 = 0$, $x_M = L$, $t_1 = 0$, $t_N = T$, M is the number of measurement points, and N is the total number of snapshots of w(x,t) in the sampling process; a snapshot of w(x,t) corresponds to a column of A. The SVD of A can be expressed by [12]

$$A = USV^{T}$$
(3)

where the subscript ^T denotes a transpose operator; U is an $M \times M$ orthogonal matrix containing all the left singular vectors of unit norms and V is an $N \times N$ orthogonal matrix containing all the right singular vectors of unit norms, and S is an $M \times N$ diagonal matrix containing all the singular values; the *i*th left and right singular vectors are denoted by \mathbf{u}_i and \mathbf{v}_i , respectively.

Let λ_i denote the *i*th singular values of **A**, and all λ_i in **S** are numbered in a descending order such that $\lambda_1 \ge \lambda_2 \ge \cdots \ge \lambda_M$. The SVD in Eq. (3) aligns well with the POD in Eq. (1) by rewriting Eq. (3) as

$$\mathbf{A} = \sum_{i=1}^{M} \mathbf{u}_i \left(\lambda_i \mathbf{v}_i^{\mathrm{T}} \right) \tag{4}$$

and \mathbf{u}_i and $\lambda_i \mathbf{v}_i^{\mathrm{T}}$ can be considered as discrete $\phi_i(x)$ and $a_i(t)$, respectively. The *i*th POM, i.e., \mathbf{u}_i , is an *M*-dimensional column vector of a unit norm and corresponds to the spatial characteristics of \mathbf{A} . The term $\lambda_i \mathbf{v}_i^{\mathrm{T}}$ is an *N*-dimensional row vector and is directly related to the contribution of \mathbf{u}_i to the formation of \mathbf{A} at different instants. Further, the contribution of \mathbf{u}_i can be quantified by λ_i since \mathbf{v}_i has a unit norm and

$$\left\|\lambda_{i}\mathbf{v}_{i}^{\mathsf{T}}\right\|_{2} = \lambda_{i}\left\|\mathbf{v}_{i}^{\mathsf{T}}\right\|_{2} = \lambda_{i} \tag{5}$$

where $\|\cdot\|_2$ calculate the L^2 -norm of a vector. Hence \mathbf{u}_i associated with a larger value of λ_i has a higher contribution to the formation of \mathbf{A} . When small-extent damage occurs to the structure, local anomalies will exist in \mathbf{A} in the neighborhood of the damage, and they derive from \mathbf{u}_i associated with \mathbf{A} .

2.2. Intensified local anomalies by CWT

The CWT with Gaussian wavelet functions is used to suppress global trends and intensify local anomalies in POMs of the guided wavefield, i.e., $\phi(x)$. The *p*th-order Gaussian wavelet function is derived from the Gaussian function, denoted by g(x), with a unit L^2 -norm and it can be expressed by [19]

$$g^{(p)}(x) = C_p \frac{\mathrm{d}^p(g(x))}{\mathrm{d}x^p} \tag{6}$$

where the superscript $^{(p)}$ denotes the pth-order spatial differentiation, C_p is a constant with which $g^{(p)}(x)$ has a unit L^2 -norm. The Gaussian function is expressed by

$$g(x) = \sqrt[4]{\frac{2}{\pi}}e^{-x^2} \tag{7}$$

The value of p can be defined as the number of vanishing moments of $g^{(p)}(x)$, and one has [20]

$$\int_{-\infty}^{\infty} x^n g^{(p)}(x) \, \mathrm{d}x = 0, \quad n = 0, 1, \dots, p - 1$$
 (8)

Further, the concept can be extended to a (p-1)th-order polynomial, i.e., $\sum_{k=0}^{p-1} c_k x^k$, such that

$$\int_{-\infty}^{\infty} \sum_{k=0}^{p-1} c_k x^k g^{(p)}(x) \, \mathrm{d}x = 0 \tag{9}$$

where c_k is the kth coefficient of the polynomial. A family of Gaussian wavelet functions associated with $g^{(p)}(x)$ can be defined and expressed by

$$g_{u,s}^{(p)}(x) = \frac{1}{\sqrt{s}}g^{(p)}\left(\frac{x-u}{s}\right)$$
 (10)

where s > 0 is termed as a scale parameter and $u \in \mathbb{R}$ a translation parameter. The Gaussian wavelet functions in Eq. (10) with a certain value of s have a finite interval, denoted by $[-\epsilon + u, \epsilon + u]$, and one has $g_{u,s}^{(p)}(x) \approx 0$ outside the interval. The interval can be termed as the non-zero interval of $g_{u,s}^{(p)}(x)$ and its width is defined to be equal to 2ϵ and the value of ϵ is directly related to that of s. Note when discrete data are processed, $g_{u,s}^{(p)}(x)$ is generated on a discrete grid, and the number of points in the non-zero interval can be approximated as [(6s + 3)], where $[\cdot]$ rounds a number up to the nearest integer.

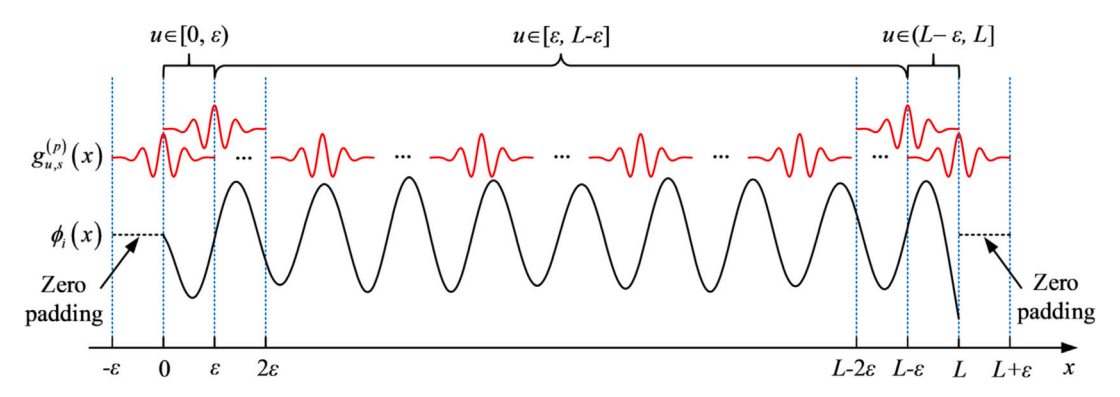


Fig. 1. Schematic of the piecewise form of $W_i(u, s)$ in Eq. (13). The function $g_{u,s}^{(p)}(x)$ has a finite non-zero interval 2ϵ and zero is padded to $\phi_i(x)$ for $x \in [-\epsilon, 0]$ and $x \in [L, L + \epsilon]$.

By substituting $g_{\mu,\nu}^{(p)}(x)$ for $g^{(p)}(x)$ in Eq. (9) and considering the existence of the non-zero interval of $g_{\mu,\nu}^{(p)}(x)$, one has

$$\int_{-\infty}^{\infty} \sum_{k=0}^{p-1} c_k x^k g_{u,s}^{(p)}(x) \, \mathrm{d}x = \int_{-\varepsilon+u}^{\varepsilon+u} \sum_{k=0}^{p-1} c_k x^k g_{u,s}^{(p)}(x) \, \mathrm{d}x = 0$$
 (11)

A CWT coefficient of $\phi_i(x)$ with $g^{(p)}(x)$ being the wavelet function can be defined and expressed by

$$W_i(u,s) = \int_{-\infty}^{\infty} \phi_i(x) \, g_{u,s}^{(p)}(x) \, \mathrm{d}x = \int_{0}^{L} \phi_i(x) \, g_{u,s}^{(p)}(x) \, \mathrm{d}x \tag{12}$$

with $u \in [0, L]$, and $W_i(u, s)$ can be rewritten in a piecewise form:

$$W_{i}(u,s) = \begin{cases} \int_{0}^{\epsilon+u} \phi_{i}(x) g_{u,s}^{(p)}(x) dx, & u \in [0,\epsilon) \\ \int_{-\epsilon+u}^{\epsilon+u} \phi_{i}(x) g_{u,s}^{(p)}(x) dx, & u \in [\epsilon, L-\epsilon] \\ \int_{-\epsilon+u}^{L} \phi_{i}(x) g_{u,s}^{(p)}(x) dx, & u \in (L-\epsilon, L] \end{cases}$$

$$(13)$$

The piecewise form is depicted in Fig. 1.

In the piecewise form, when $u \in [\varepsilon, L - \varepsilon]$, $\phi_i(x)$ with $x \in [-\varepsilon + u, \varepsilon + u]$ can be written as a sum of three components, including the global trend $\hat{\phi}_i(x)$, local anomalies $\tilde{\phi}_i(x)$, if existing, and white noise $\bar{\phi}_i(x)$, if existing, and $\phi_i(x)$ can be expressed by

$$\phi_i(x) = \hat{\phi}_i(x) + \tilde{\phi}_i(x) + \tilde{\phi}_i(x) \tag{14}$$

Assume that $\hat{\phi}_i(x)$ be well approximated by a dth-order polynomial such that

$$\hat{\phi}_i(x) = \sum_{k=0}^{d} c_k x^k \tag{15}$$

Substituting Eqs. (14) and (15) into Eq. (13), $W_i(u, s)$ with $u \in [\epsilon, L - \epsilon]$ can be rewritten as

$$W_{i}(u,s) = \int_{-\epsilon+u}^{\epsilon+u} \sum_{k=0}^{d} c_{k} x^{k} g_{u,s}^{(p)}(x) dx + \int_{-\epsilon+u}^{\epsilon+u} \tilde{\phi}_{i}(x) g_{u,s}^{(p)}(x) dx + \int_{-\epsilon+u}^{\epsilon+u} \bar{\phi}_{i}(x) g_{u,s}^{(p)}(x) dx$$
 (16)

If $d \le p-1$, the first term in Eq. (16), i.e., $\int_{-\epsilon+u}^{\epsilon+u} \sum_{k=0}^{d} c_k x^k g_{u,s}^{(p)}(x) dx$, vanishes based on Eq. (11) and one has

$$W_{i}(u,s) = \int_{-c+u}^{c+u} \tilde{\phi}_{i}(x) g_{u,s}^{(p)}(x) dx + \int_{-c+u}^{c+u} \bar{\phi}_{i}(x) g_{u,s}^{(p)}(x) dx$$
 (17)

By the application of the CWT to $\phi_i(x)$ with $g_{u,s}^{(d+1)}(x)$, the effects of $\hat{\phi}_i(x)$ on $W_i(u,s)$ can be suppressed while those of $\tilde{\phi}_i(x)$ and $\tilde{\phi}_i(x)$ are retained.

The modulus of $W_i(u, s)$ is expressed by

$$\begin{aligned} \left| W_{i}(u,s) \right| &= \left| \int_{-\epsilon+u}^{\epsilon+u} \tilde{\phi}_{i}(x) g_{u,s}^{(p)}(x) \, \mathrm{d}x + \int_{-\epsilon+u}^{\epsilon+u} \bar{\phi}_{i}(x) g_{u,s}^{(p)}(x) \, \mathrm{d}x \right| \\ &\leq \left| \int_{-\epsilon+u}^{\epsilon+u} \tilde{\phi}_{i}(x) g_{u,s}^{(p)}(x) \, \mathrm{d}x \right| + \left| \int_{-\epsilon+u}^{\epsilon+u} \bar{\phi}_{i}(x) g_{u,s}^{(p)}(x) \, \mathrm{d}x \right| \end{aligned} \tag{18}$$

where $|\cdot|$ denotes an absolute value. Singularities exist in $\tilde{\phi}_i(x)$ at damage areas of a structure and the value of $\tilde{\phi}_i(x)$ vanishes at otherwise intact areas of the structure. The modulus of wavelet coefficient of $\tilde{\phi}_i(x)$, i.e., $\left|\int_{-\varepsilon+u}^{\varepsilon+u} \tilde{\phi}_i(x) \, g_{u,s}^{(p)}(x) \, dx\right|$, increases with the value of s in the neighborhoods of the damage [21]. However, the modulus of wavelet coefficient of white noise,

i.e., $\left| \int_{-\epsilon+u}^{\epsilon+u} \bar{\phi}_i(x) g_{u,s}^{(p)}(x) dx \right|$, decreases as the value of s increases [21]. Therefore, there exists a threshold scale parameter denoted by s_0 such that

$$\left| \int_{-\epsilon+u}^{\epsilon+u} \bar{\phi}_i(x) g_{u,s_0}^{(p)}(x) \, \mathrm{d}x \right| \ll 1 \tag{19}$$

and when $s \ge s_0$, one has

$$\left| W_i(u,s) \right| \approx \left| \int_{-\epsilon+u}^{\epsilon+u} \tilde{\phi}_i(x) g_{u,s}^{(p)}(x) \, \mathrm{d}x \right| \tag{20}$$

Note that adverse effects of $\tilde{\phi}_i(x)$ on $|W_i(u,s)|$ with $u \in [\varepsilon, L - \varepsilon]$ for damage identification are suppressed when $s \geqslant s_0$, and more importantly, the existence of $\tilde{\phi}_i(x)$ is localized and amplified.

While the integral interval of $W_i(u,s)$ in Eq. (12) is equal to 2ϵ , this condition cannot be directly satisfied when $u \in [0,\epsilon)$ as the available $\phi_i(x)$ has a length of $\epsilon + u$. Hence, zero with a length of $\epsilon - u$ is padded to the low end $\phi_i(x)$ so that the width of the associated integral interval of $W_i(u,s)$ becomes 2ϵ . In Eq. (13), when $u \in [0,\epsilon)$, $\phi_i(x)$ with $x \in [-\epsilon + u, \epsilon + u]$ also consists of three components, including $\hat{\phi}_i(x)$, $\tilde{\phi}_i(x)$ and $\bar{\phi}_i(x)$. However, the order of a polynomial that well approximates the zero-padded $\hat{\phi}_i(x)$ will be greatly larger than those for $\hat{\phi}_i(x)$ with $u \in [\epsilon, L - \epsilon]$. If the value of p is determined based on $\hat{\phi}_i(x)$ with $u \in [\epsilon, L - \epsilon]$, the effects of the zero-padded $\hat{\phi}_i(x)$ on $W_i(u,s)$ cannot be well suppressed with $u \in [0,\epsilon)$, which leads to large $|W_i(u,s)|$ values even when a structure is intact in $u \in [0,\epsilon)$. This phenomenon is termed the edge-effect of wavelet transforms [22]. Similarly, the edge-effects occur to $W_i(u,s)$ with $u \in [L - \epsilon, L]$ due to the zero-padding to the high end of $\phi_i(x)$ with $x \in [L, L + \epsilon]$.

2.3. Damage identification process

2.3.1. Truncation for significant POMs

Damage sensitivity of structural characteristic deflection shapes, such as mode shapes and operational deflection shapes [23], depends on locations and extent of damage [24]. Hence, one structural characteristic deflection shape can be insensitive to certain damage or it cannot fully indicate the extent of the damage, which is analogous to POMs of guided wavefields. In practice, one should not use all available POMs of a guided wavefield for damage identification. The reason is that noise dominates small singular values [25], and their associated POMs have a small signal-to-noise ratio (SNR), which can lead to false-positive damage identification results. Hence, it is desirable to truncate the POMs such that significant POMs are used for damage identification to reveal the local anomalies with higher confidence. Hence an adaptive truncation technique is developed here to determine the number of POMs to be used for damage identification.

In the truncation technique, an empirical threshold is defined to identify the significant POMs. The empirical threshold is determined to be

$$\tau_o = \lambda_1 \times 5\% \tag{21}$$

and the number of significant POMs is determined to be

$$r = \arg\min_{i} \left(\lambda_i - \tau_e \right), \quad \lambda_i \geqslant \tau_e$$
 (22)

The empirical threshold assumes that POMs with λ_i less than 5% of λ_1 can be related to measurement noise and should be excluded for damage identification.

2.3.2. Determining proper orders of Gaussian wavelet functions

Similar to Ref. [26], the modal assurance criterion value is used to construct $\hat{\phi}_i(x)$ from $\phi_i(x)$ with $x \in [-\epsilon + u, \epsilon + u]$, which can be calculated by [27]

$$MAC\left(\phi_{i}\left(x\right),\hat{\phi}_{i}\left(x\right)\right) = \frac{\left(\hat{\phi}_{i}\left(x\right)^{T}\phi_{i}\left(x\right)\right)^{2}}{\left(\hat{\phi}_{i}\left(x\right)^{T}\hat{\phi}_{i}\left(x\right)\right)\left(\phi_{i}\left(x\right)^{T}\phi_{i}\left(x\right)\right)} \times 100\%$$
(23)

and $\hat{\phi}_i(x)$ is determined by a polynomial in Eq. (15) with the minimum order d with which MAC is greater than 90%. When all $\hat{\phi}_i(x)$ in $\phi_i(x)$ with $x \in [-\epsilon + u, \epsilon + u]$ are determined, where $u \in [\epsilon, L - \epsilon]$ and $i \in \{1, 2, ..., r\}$, the orders of the polynomials for all $\hat{\phi}_i(x)$, i.e., all obtained d, can be constructed as a two-dimensional matrix \mathbf{d} . If a structure is subject to an excitation force that has finite frequency components, the spatial frequency of measured guided waves will have finite frequency components such that a majority of $\hat{\phi}_i(x)$ for significant $\phi_i(x)$ with $x \in [-\epsilon + u, \epsilon + u]$ can be well fitted by polynomials with similar orders. In other words, the majority of entries of \mathbf{d} will be smaller than a certain threshold value. Meanwhile, there exist outliers of entries of \mathbf{d} that are larger than the threshold value possibly due to the existence of local anomalies and noise as $\hat{\phi}_i(x)$ are constructed based on $\phi_i(x)$.

Assuming that the entries of \mathbf{d} are well spread in a normal distribution, a statistical criterion is applied to assist determination of the proper value of p. In the criterion, the upper bound in two standard deviations of the mean of the distribution is used and it is calculated by

$$\tau_p = \mu + 2\sigma \tag{24}$$

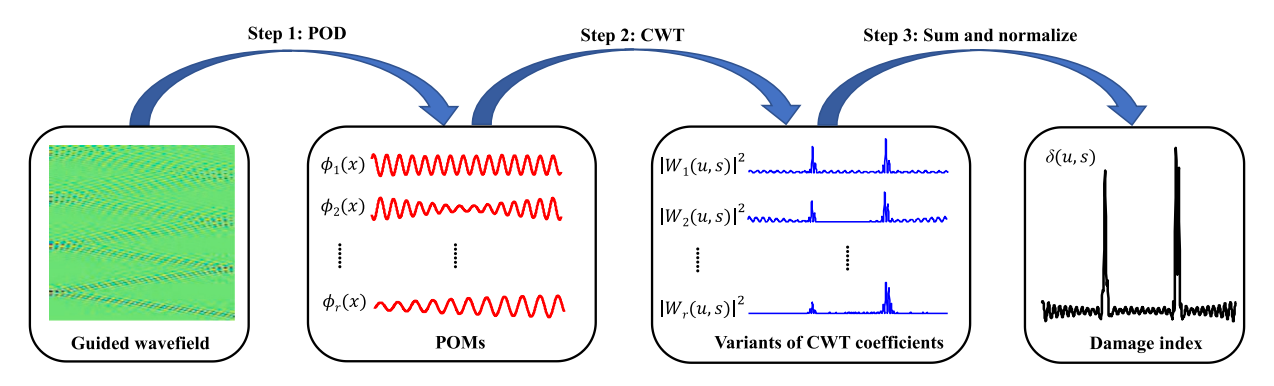


Fig. 2. Flowchart of the proposed damage identification method.

where μ and σ denote the mean and standard deviation of all the entries of \mathbf{d} , respectively. Note that 97.7% of entries of \mathbf{d} are not greater than τ_p [28]. The criterion is capable of effectively ruling out the outliers in \mathbf{d} when determining the proper value of p. When $p = \lceil \tau_p \rceil + 1$, the effects of the majority of $\hat{\phi}_i(x)$ on $W_i(u,s)$ can be suppressed. However, when p is equal to an odd value and an even one, the resulting $W_i(u,s)$ displays zero-crossings and local extrema at the locations of structural damage, respectively. To intensify the existence of damage as large values in the damage index to be formulated based on $W_i(u,s)$, it is proposed that the proper value of p be an even value that is calculated by

$$p = 2\left\lceil \frac{\tau_p + 1}{2} \right\rceil \tag{25}$$

2.3.3. Accumulative damage index

After determining the proper values of r and p using Eqs. (22) and (25), respectively, an accumulative damage index can be constructed for damage identification. It is defined based on $|W_i(u,s)|$ with the pth order Gaussian functions associated with r significant POMs:

$$\delta(u,s) = \frac{\sum_{i=1}^{r} |W_i(u,s)|^2}{\max \sum_{i=1}^{r} |W_i(u,s)|^2}$$
(26)

where $|W_i(u,s)|^2$ is used for further suppressing the effects of global trends and intensifying those of local anomalies. Note that $\delta(u,s) \in [0,1]$ and damage can be identified in neighborhoods with relatively high values of $\delta(u,s)$ when $s > s_0$. However, there is no universally proper value of s_0 due to the fact that it depends on the unknown noise level of w(x,t). A feasible practice is to present $\delta(u,s)$ with a monotonically increasing value of s. An appropriate s is the one beyond which consistent damage identification results are observed. Besides, w(x,t) is obtained with M measurement points in $x \in [0,L]$. As $g_{u,s}^p(x)$ is generated on the discrete grid, w(x,t) needs to be mapped to the discrete grid in the spatial domain. In other words, w(x,t) is obtained by uniform sampling at unit intervals in the spatial domain. Hence, $W_i(u,s)$ are calculated at scales $s \in (1,M)$ [29]. In this study, the values of $\delta(u,s)$ are calculated in $s \in [2,20]$ for the numerical and experimental investigations. A flowchart summarizing the proposed damage identification method is shown in Fig. 2.

3. Numerical investigation

In this section, guided wavefields obtained from numerical simulations of an aluminum cantilever beam with damage in the forms of two thickness reduction areas are studied by applying the proposed damage identification method. The effectiveness and noise-robustness of the method is investigated and discussed.

3.1. Numerical model of a damaged aluminum cantilever beam

The aluminum cantilever beam has a length of 300 mm, a width of 3 mm, and a height of 6 mm and its numerical model is constructed using the finite element modeling software ABAQUS. Two one-sided through-width thickness reduction areas with a depth of 0.3 mm are introduced to the specimen as damage. Dimensions of the beam and the locations of the damage are shown in Fig. 3. The damaged beam is made of aluminum with a mass density of 2700 kg/m³, Young's modulus of 68.9 GPa, Poisson's ratio of 0.33, and zero damping. The model of the damaged beam is built with the linear eight-node brick (C3D8R) elements. The damaged beam is under zero initial conditions and subject to an N_c -count wave packet force applied to the damaged side of the free end of the beam. The force can be analytically expressed by

$$h(t) = A\left(H(t) - H\left(t - \frac{N_c}{f_c}\right)\right) \left(1 - \cos\left(\frac{2\pi f_c t}{N_c}\right)\right) \sin\left(2\pi f_c t\right)$$
(27)

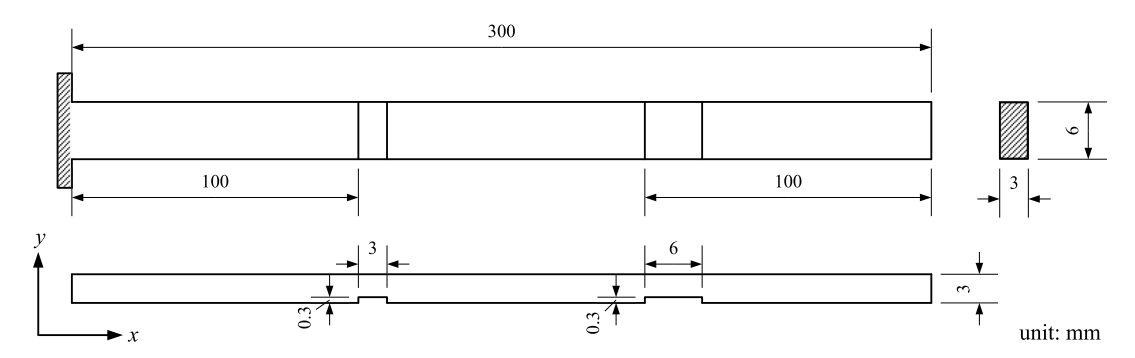


Fig. 3. Dimensions of the simulated damaged aluminum beam with two thickness reduction areas.

where A defines the magnitude of the force, H is the Heaviside function expressed by

$$H(t) = \begin{cases} 1, & t \ge 0 \\ 0, & t < 0 \end{cases}$$
 (28)

and f_c is the central frequency of the force. The values of A and N_c are chosen to be 0.5 N and 5, respectively, and four force scenarios with different f_c values, including 30 kHz, 50 kHz, 70 kHz, and 90 kHz, are selected in this investigation.

A guided wavefield of the damaged beam is obtained on a grid with 1001 measurement points that are evenly distributed along the length of the intact side of the beam with a sampling frequency of 1.25 MHz. The measurement lasts for 2 ms after the excitation force is applied. A total of 2501 snapshots are obtained in each excitation scenario. Guided wavefields in the first 0.5 ms with $f_c = 30$ kHz, 50 kHz, 70 kHz, and 90 kHz are shown in Figs. 4(a) through (d), respectively. Fig. 4(a) shows the guided wavefield consists of a guided wave generated from the free end, propagating toward the fixed end, and reflecting back and forth at the ends of the beam. Reflections cannot be directly observed near the edges of the two damage areas, possibly due to their magnitudes being too small. In Figs. 4(b) through (d), similar observations can be made regarding the three guided wavefields.

3.2. Numerical damage identification results

The effectiveness of the proposed damage identification method is investigated numerically based on the four guided wavefields of the damaged beam. The use of snapshots in the whole sampling period can lead to false-positive identification results that local anomalies exist near an excitation point [2]. To exclude the false-positive results by the proposed method, only snapshots after [26]

$$t_1 = t_e + t_p \tag{29}$$

are used for POD, where t_e and t_p denote the ending instant and duration of h(t) in Eq. (27), respectively. Values of t_1 associated with the four wavefields are listed in Table 1. Singular values of the wavefield associated with $f_c = 30$ kHz are plotted in Fig. 5(a). It can be seen that only the first ten singular values are larger than τ_e in Eq. (21), and the number of significant $\phi_i(x)$, i.e., r, for the wavefield is ten. The value of r for the other three guided wavefields is determined and listed in Table 1. The matrix \mathbf{d} for the ten significant $\phi_i(x)$ is estimated and its entries for s=8 are shown in Fig. 5(b). It can be seen that the value of d is equal to either one or two, indicating that $\hat{\phi}_i(x)$ for the significant $\phi_i(x)$ with $x \in [-\epsilon + u, \epsilon + u]$ are well fitted by first- or second-orders polynomials. The proper orders of Gaussian wavelet functions, i.e., p, with integer $s \in [2,20]$ are determined and plotted in Fig. 5(c). When $f_c = 30$ kHz, the values of p are equal to 4, 6 and 8 when $s \in [2,10]$, [11,17] and [18,20], respectively, and two boundaries exist at s = 10 and 17, as shown in Fig. 5(c). When, $f_c = 50$ kHz, a similar observation can be made: the values of p are equal to different values when s fall in different ranges and three boundaries exist s = 8, 13 and 19; such similar observations can be made when $f_c = 70$ and 90 kHz, where s ranges and boundaries differ from the other two scenarios. The observations verify that the value of p might increase with s and s0, since an increase of s1 will increase the length of s1, s2, ince, and that of s2, will increase the spatial frequency of s3, increasing either of 2s6 or the spatial frequency of s3, including a polynomial with a higher order to well approximate s3, increasing either of 2s6 or the spatial frequency of s3, increasing either of 2s6 or the spatial frequency of s3, increasing either of 2s6 or the spatial frequency of s3, increasing either

Damage indexes based on Eq. (26) are obtained and shown in Fig. 6. In Fig. 6(a), consistently high $\delta(u, s)$ values can be observed, where the locations and extent of the damage are identified. Besides, a part of $\delta(u, s)$ values beyond damage areas increase with s and it is interesting to notice that the increasing trend of $\delta(u, s)$ exists in three different s ranges and they are the same as those observed in Fig. 5(c), where p values increases in different s ranges. This is because increasing the value of s can increase the length of $\hat{\phi}_i(x)$, i.e., 2ϵ , and the effect of $\hat{\phi}_i(x)$ on $W_i(u, s)$ cannot be suppressed completely by the same p value in $g_{u,s}^{(p)}(x)$. In Figs. 6(b) through (d), similar damage identification results are obtained, where consistently high $\delta(u, s)$ are observed in damage areas, and the increasing trend of $\delta(u, s)$ exists in different s ranges. The zoomed-in views of $\delta(u, s)$ obtained from the guided wavefield with $f_c = 50$ kHz nearby two damage areas are shown in Figs. 6(e) and (f). It can be seen that high $\delta(u, s)$ values mainly exist in the two damage areas so that the consistently high $\delta(u, s)$ values can accurately identify the locations and extent of the damage.

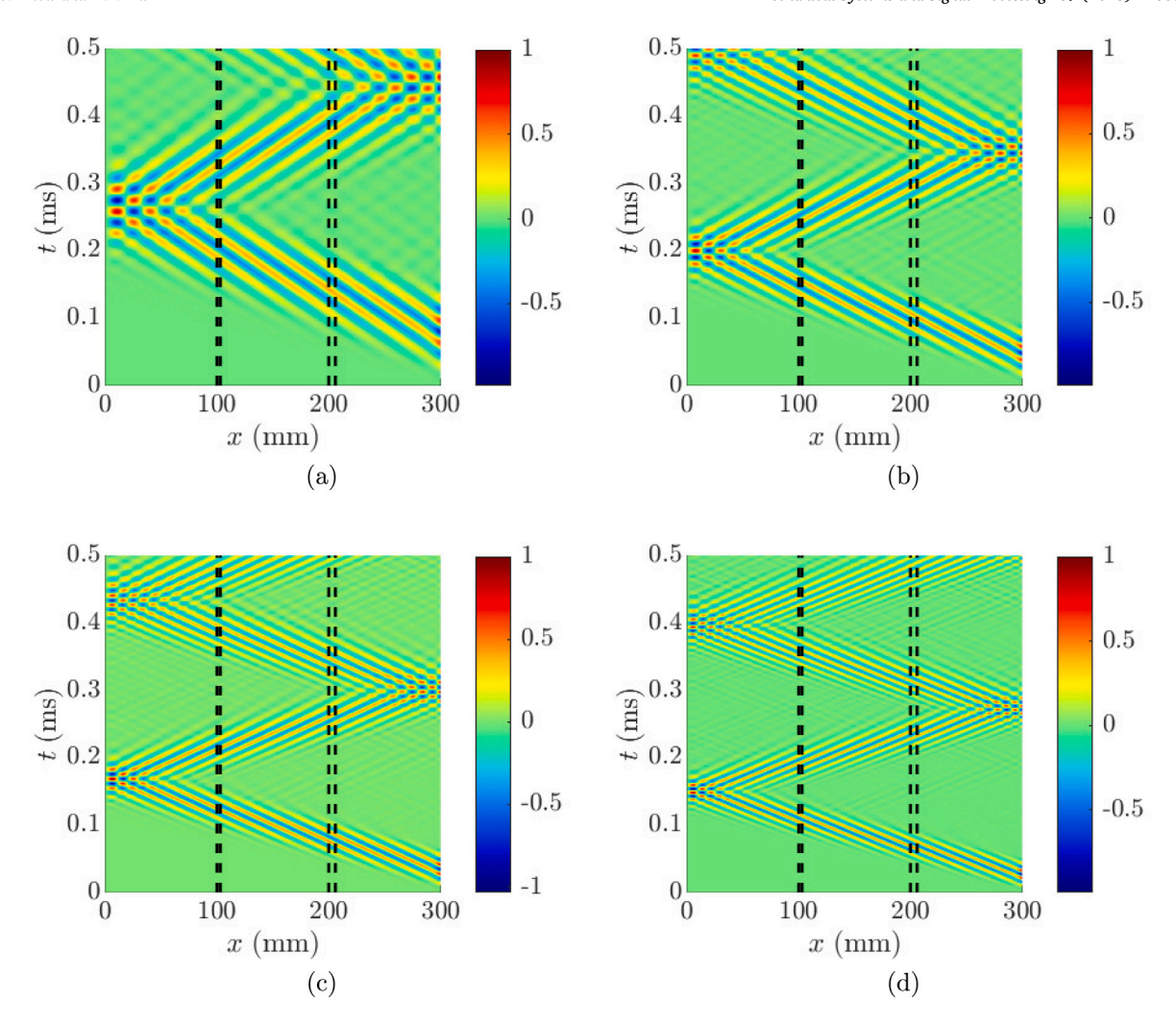


Fig. 4. Guided wavefields of the damaged beam in the first 0.5 ms with f_c being (a) 30 kHz, (b) 50 kHz, (c) 70 kHz and (d) 90 kHz. Edges of the two damage areas are depicted by vertical dotted lines. For better comparison, the amplitudes of the guided wavefield shown in each figure are normalized so that its maximum value is equal to one.

Table 1 The determined values of t_1 and number of significant $\phi_i(x)$, i.e., r for the numerical investigation and experimental validation.

f_c (kHz)	Numerical investigation		Experimental validation	
	t ₁ (ms)	r	t_1 (ms)	r
30	0.3344	10	0.6560	25
50	0.2000	13	0.5128	53
70	0.1440	16	0.4536	56
90	0.1120	18	0.4200	61

To investigate the noise robustness of the proposed method, white Gaussian noise is added to the guided wavefield with $f_c=50$ kHz at four noise levels such that the resulting four noise-contaminated guided wavefields have SNRs of 50 dB, 45 dB, 40 dB and 35 dB. Fig. 7 shows $\delta(u,s)$ obtained from the noise-contaminated guided wavefields. In Fig. 7(a) and its zoomed-in views Figs. 7(e) and (f), when s<3 consistently high $\delta(u,s)$ values are observed on the damaged and intact areas of the beam, and the damage cannot be identified based on $\delta(u,s)$. However, when $s\geq3$ consistently high $\delta(u,s)$ values can be observed solely in the neighborhoods of the damage, and the locations and extent of the damage can be identified. It is verified that the effects of $\bar{\phi}_i$ can be well suppressed by increasing the value of s and the value of s_0 in Eq. (19) is close to 3 for the guided wavefield with the SNR of 50 dB. In Figs. 7(b) through (d), damage can also be identified based on consistently high $\delta(u,s)$ values. Besides, it can be seen that the value of s_0 is

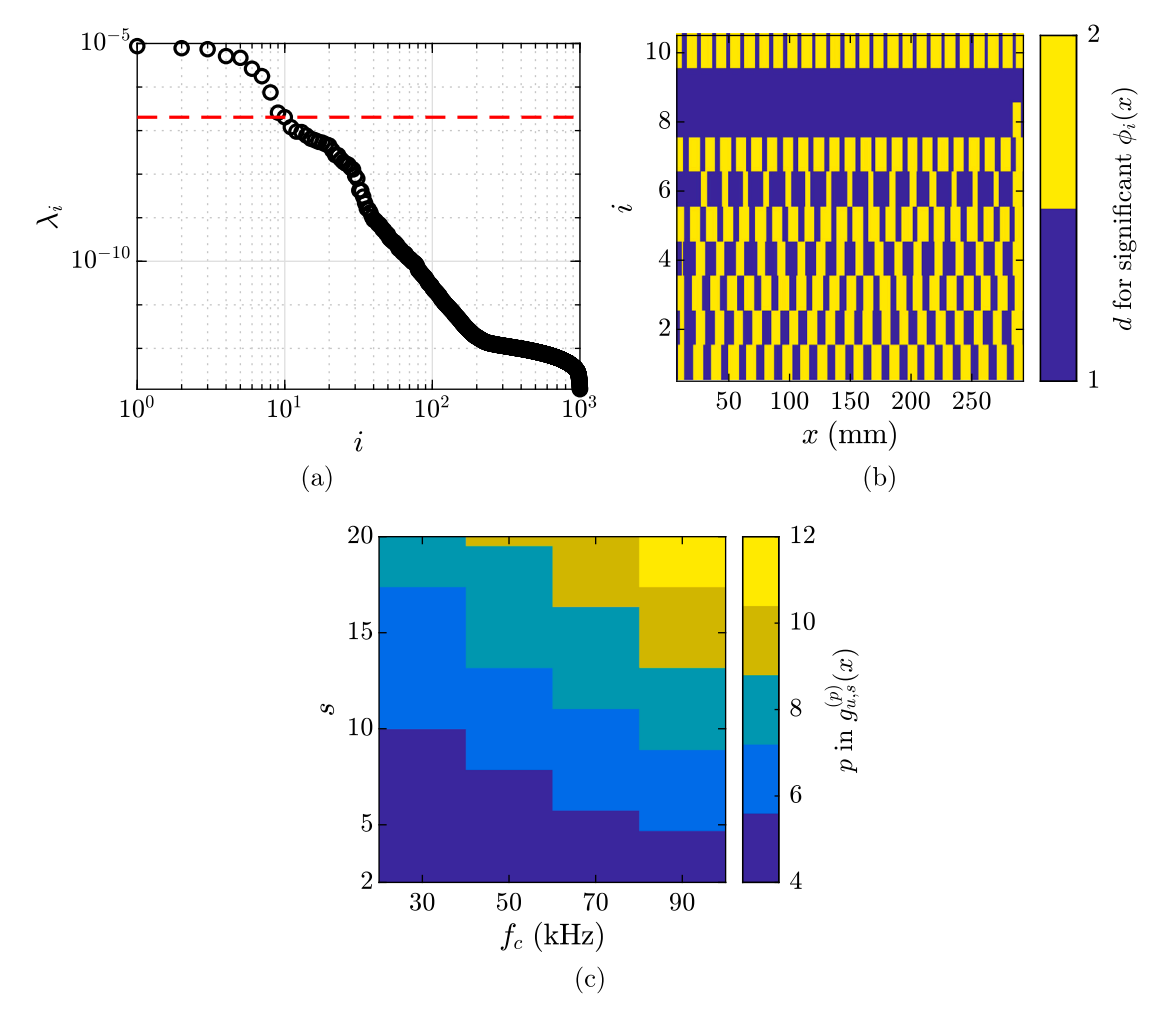


Fig. 5. (a) Singular values of the guided wavefield with $f_c = 30$ kHz, (b) the value of d for significant $\phi_i(x)$ of the guided wavefield with $f_c = 30$ kHz when s = 8 and (c) p for suppressing $\hat{\phi}_i(x)$ for the four guided wavefields in the numerical investigation. The empirical threshold for determining significant $\phi_i(x)$ is depicted by the horizontal dotted line in (a).

close to 4, 5, and 6 for the guided wavefield with the SNR of 45 dB, 40 dB and 35 dB respectively, which increases with the noise level.

4. Experimental validation

In this section, experimental investigations on the effectiveness of the proposed method were conducted on a damaged aluminum cantilever beam with damage in the form of a one-sided thickness reduction area.

4.1. Experimental test specimen and its guided wavefield

The damaged aluminum cantilever beam had a length of 868 mm, a width of 25.6 mm, and a thickness of 3.5 mm. A one-sided thickness reduction area with a length of 40 mm was introduced to a side of the beam between x=408 mm and 448 mm. Dimensions of the beam and the damage area are depicted in Fig. 8(a). A schematic of the experimental setup is shown in Fig. 8(b). A STEMINC SMD07T02R412WL circular lead-zirconate-titanate (PZT) actuator was glued on the damaged side of the free end of the beam to generate excitation forces in the form of a five-count wave packet as described in Eq. (27). The excitation forces had four f_c , including 30 kHz, 50 kHz, 70 kHz and 90 kHz. A Tektronix AFG3022C function generator was used to generate the excitation forces. A Krohn-Hite 7500 amplifier was used to amplify the excitation forces to the peak-to-peak amplitude of 150 V and the amplified excitation force signals were monitored by a Tektronix TBS2104 oscilloscope. A Polytec PSV-500-HV SLDV was employed to measure guided waves on a scan line assigned to the middle of the intact side along the length of the damaged aluminum cantilever beam. A total of 3010 measurement points were evenly distributed along the scan line. The guided waves were measured with a pre-trigger of

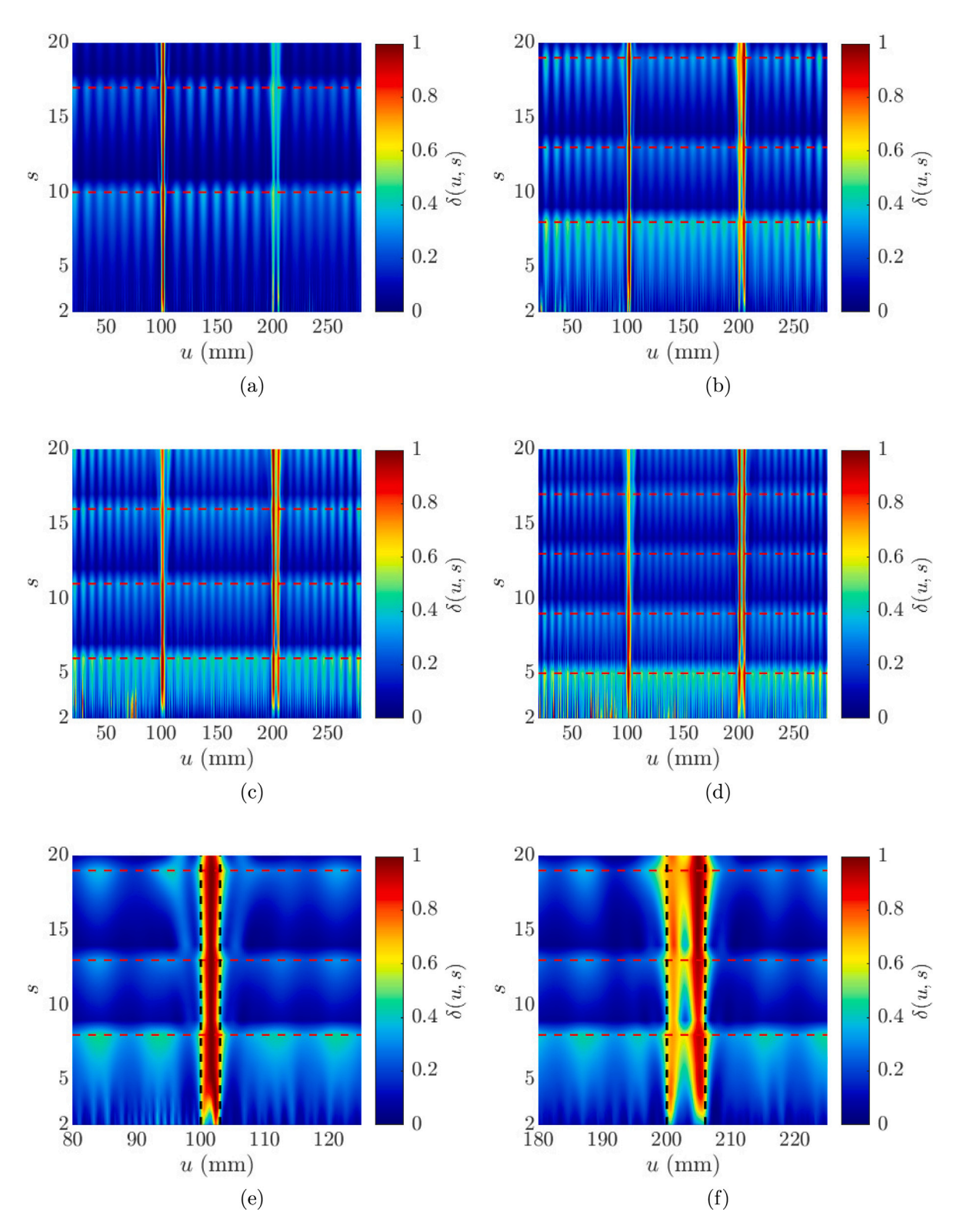


Fig. 6. Numerical damage identification results obtained from the guided wavefields with f_c being (a) 30 kHz, (b) 50 kHz, (c) 70 kHz, (d) 90 kHz, (e) a zoomed-in view of the damage area in (b) near u = 100 mm and (f) a zoomed-in view of the damage area in (b) near u = 200 mm. The boundaries of layers of values of p are depicted by the horizontal dotted lines. Edges of the two damage areas are depicted by vertical dotted lines in (e) and (f).

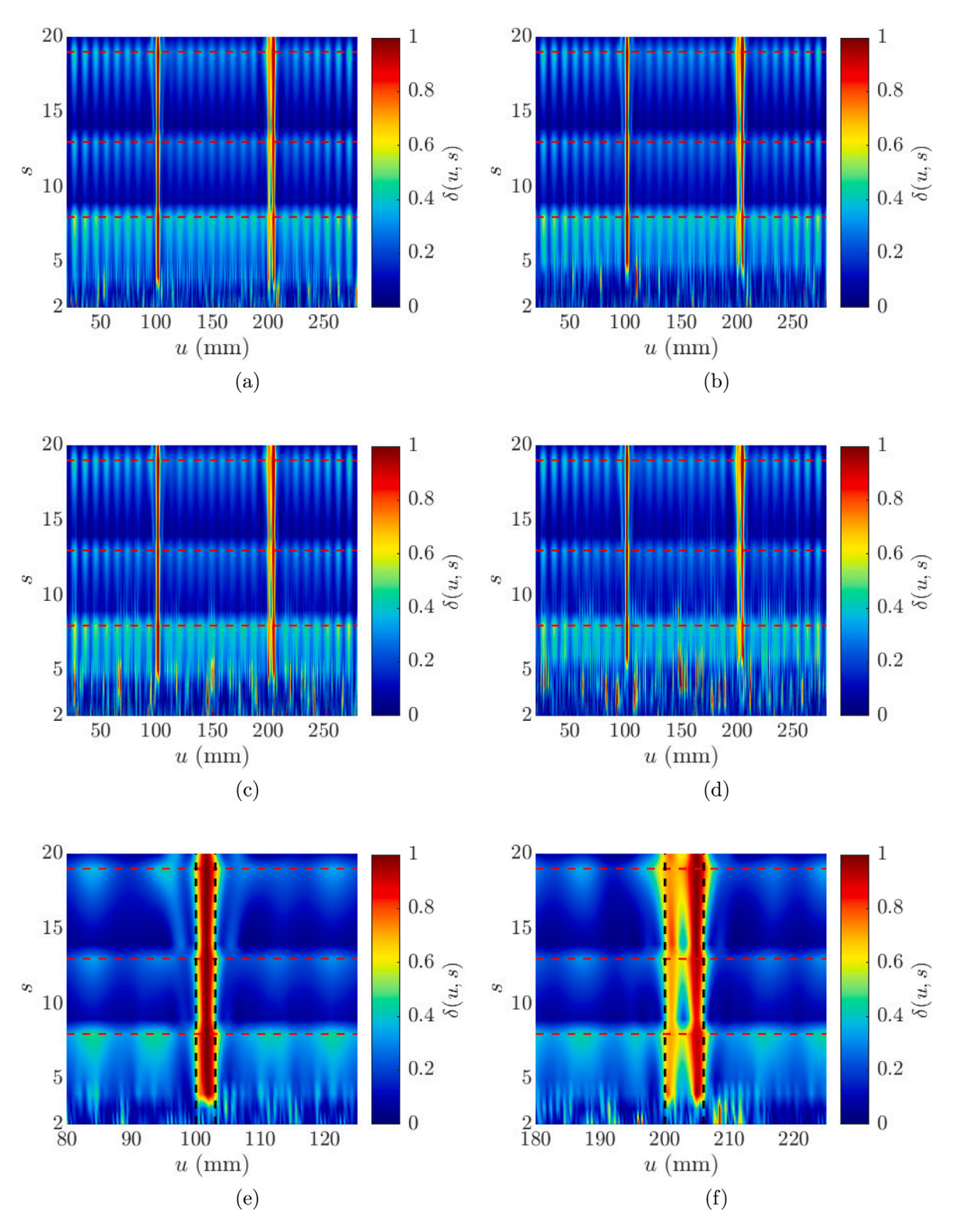


Fig. 7. Numerical damage identification results obtained from the noise-contaminated guided wavefields with SNR being (a) 50 dB, (b) 45 dB, (c) 40 dB, (d) 35 dB, (e) a zoomed-in view of the damage area in (a) near u = 100 mm and (f) a zoomed-in view of the damage area in (a) near u = 200 mm. The boundaries of layers of values of p are depicted by the horizontal dotted lines. Edges of the two damage areas are depicted by vertical dotted lines in (e) and (f).

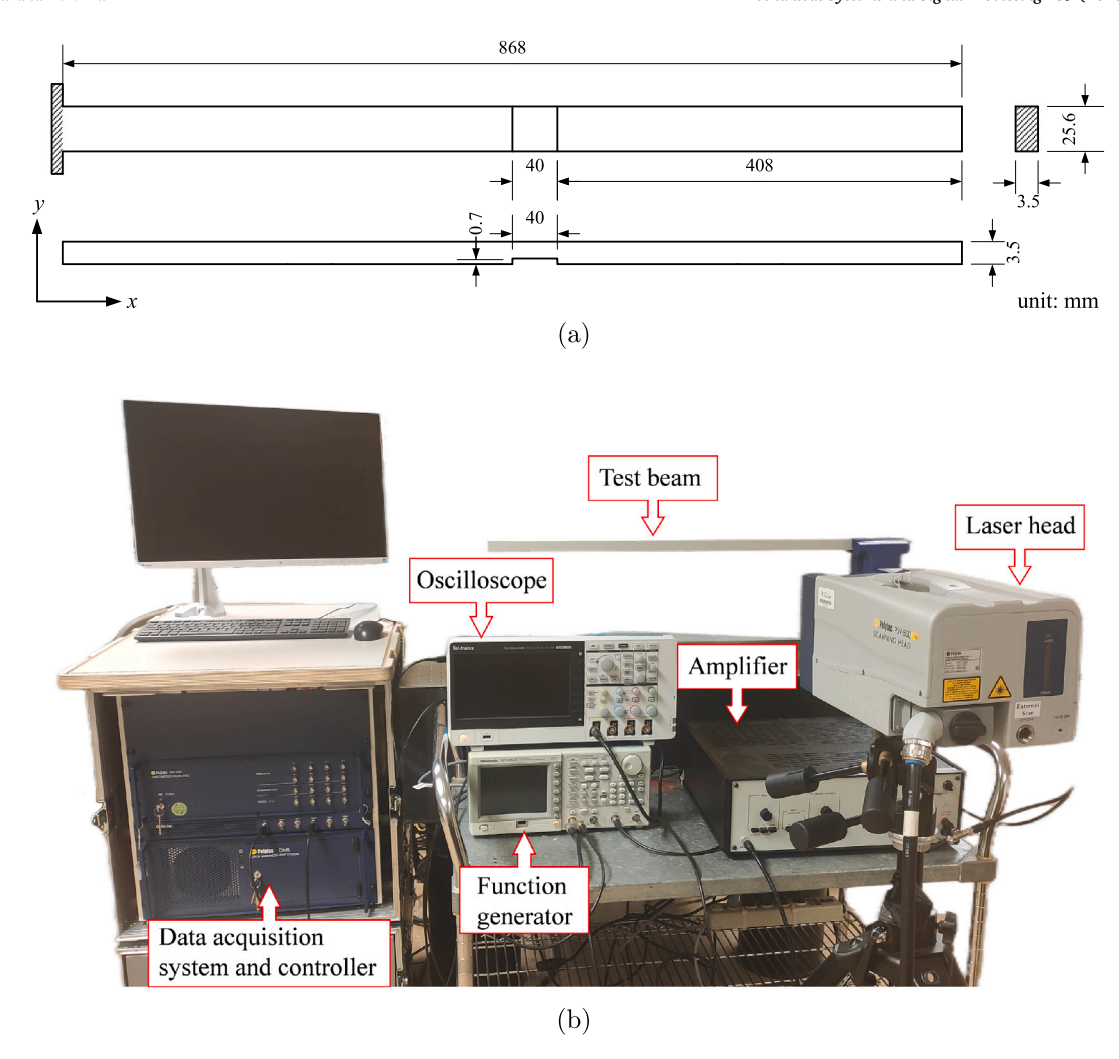


Fig. 8. (a) Dimensions of the damaged aluminum beam with a thickness reduction area in the experimental validation and (b) the schematic of the experimental setup to measure guided wavefields of the damaged aluminum beam.

0.3 ms, a sampling frequency of 1.25 MHz, a measurement period of 10 ms, and 50 averages were conducted for each measurement point. The pre-trigger was added to ensure that the guided waves of each measurement point was synchronized such that guided wavefields of the beam could be correctly presented. The averaged guided waves of all measurement points were reconstructed as a one-dimensional guided wavefield at each measurement snapshot. Two denoising techniques were used for the guided wavefields. One was a high-pass finite impulse response filter with 10 kHz cutoff frequency. The other was the numerical smoothing with weighted quadratic least squares and a first-order polynomial model, which is calculated at the measurement point within an interval that consists of 0.5% of all measurement points, i.e., 15 measurement points.

Guided wavefields of the damaged beam in the first 1.5 ms with $f_c = 30$ kHz, 50 kHz, 50 kHz, 50 kHz are shown in Figs. 9(a) through (d), respectively. Fig. 9(a) shows the guided wavefield consisted of a guided wave generated from the free end, propagating toward the fixed end, reflecting back and forth, and attenuating with t due to the existence of damping. Besides, reflections could not be easily observed near the edges of the damage area, possibly due to the amplitudes of the reflections caused by the damage being too low to be observed. However, local anomalies caused by the superposition of propagating waves and reflected waves can be observed in the damage area. In Figs. 9(b) through (d), similar observations can be made regarding the respective wavefields, but local anomalies are not obvious as those in the wavefield with $f_c = 30$ kHz.

4.2. Experimental damage identification results

The effectiveness of the proposed damage identification method was investigated experimentally based on four guided wavefields of the damaged beam, which contain snapshots after t_1 listed in Table 1. The POD was performed based on snapshots of the four

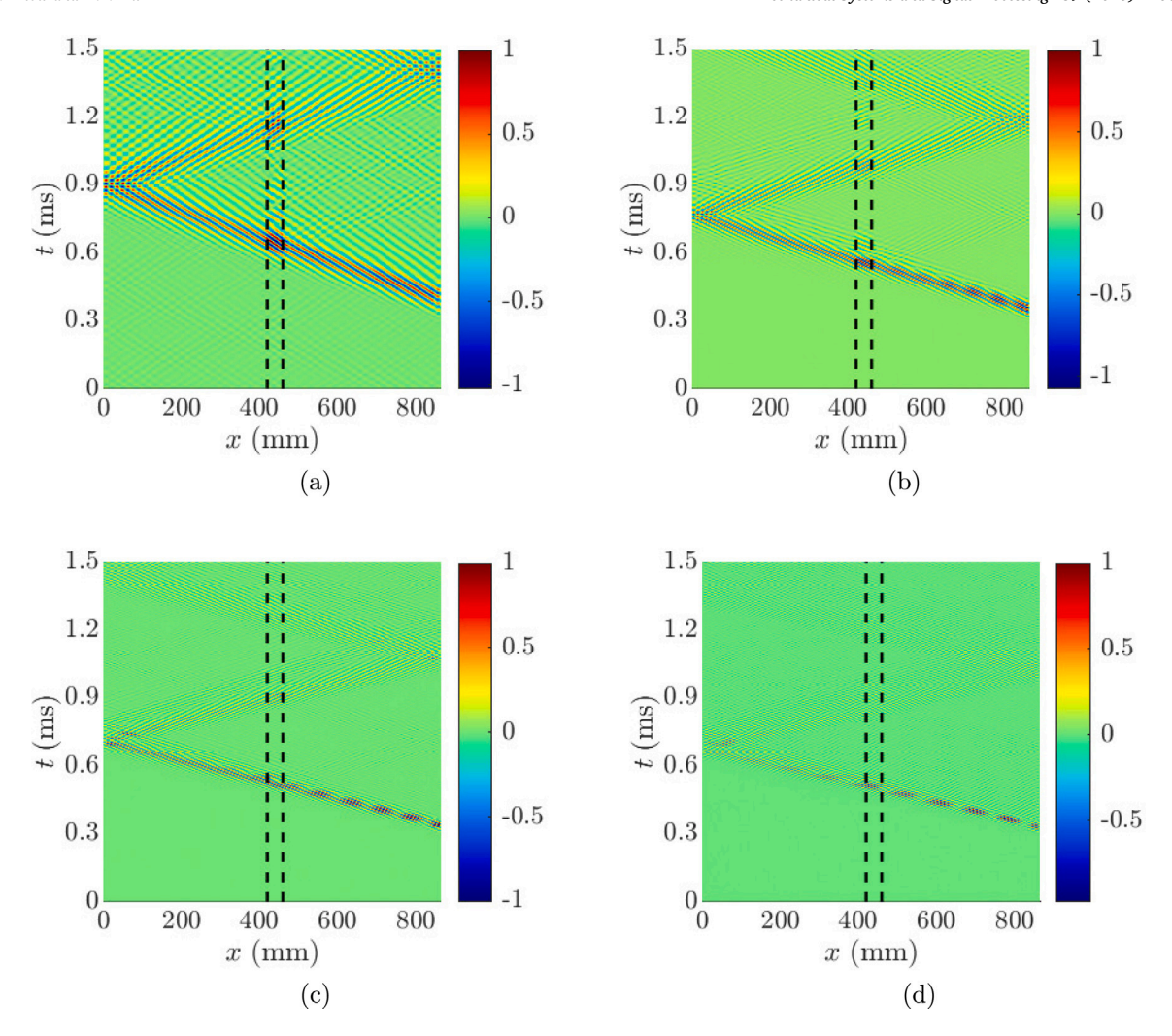


Fig. 9. Guided wavefields of the damaged beam in the first 1.5 ms with f_c being (a) 30 kHz, (b) 50 kHz, (c) 70 kHz and (d) 90 kHz. Edges of the damage area are depicted by two vertical dotted lines. For better comparison, the amplitudes of the guided wavefield shown in each figure are normalized so that its maximum value is equal to one.

guided wavefields. Fig. 10(a) shows singular values of the guided wavefield with $f_c = 30$ kHz. It can be seen that only 25 singular values were larger than τ_e in Eq. (21) so that the number of significant $\phi_i(x)$, i.e., r, for the wavefield was determined to be 25. The values of r for the other three guided wavefields were determined and listed in Table 1. The values of p with integer $s \in [2,20]$ were determined from the r significant $\phi_i(x)$ of the four guided wavefields, as shown in Fig. 10(b). When $f_c = 30$ kHz, the values of p were equal to 4, 6 and 8 when $s \in [2,10]$, [11,18] and [19,20], respectively, and two boundaries existed at s = 10 and 18, as shown in Fig. 10(c). When, $f_c = 50$ kHz, a similar observation could be made: the values of p were equal to different values when $s \in [2,10]$ in different three ranges and two boundaries existed s = 8 and 15; such similar observations could be made when $s \in [2,10]$ and 90 kHz, where the $s \in [2,10]$ ranges and boundaries differed from the other two scenarios.

Damage indexes were then calculated and shown in Fig. 11. In Figs. 11(a), consistently high $\delta(u, s)$ values could be observed when nearly $s \ge 5$, where the location and extent of the damage could be identified. The effects of noise were mainly suppressed when $s \ge 5$, but a part of effects even existed with a higher value of s. In Figs. 11(b) through (d), consistently high $\delta(u, s)$ were also observed in the neighborhoods of the damage area when nearly $s \ge 5$. Besides, a part of $\delta(u, s)$ values beyond damage areas increased with s and it is interesting to notice that the trend of increasing $\delta(u, s)$ existed in different s ranges and they were the same as those observed in Fig. 10(c), where p values increased in different s ranges. The zoomed-in views of $\delta(u, s)$ associated with the guided wavefields with $f_c = 30$ and 50 kHz centered at the damage area were shown in Figs. 11(e) and (f), respectively. It can be seen that high $\delta(u, s)$ values mainly existed in the damage area, and the consistently high $\delta(u, s)$ values could accurately identify the location and extent of the damage.

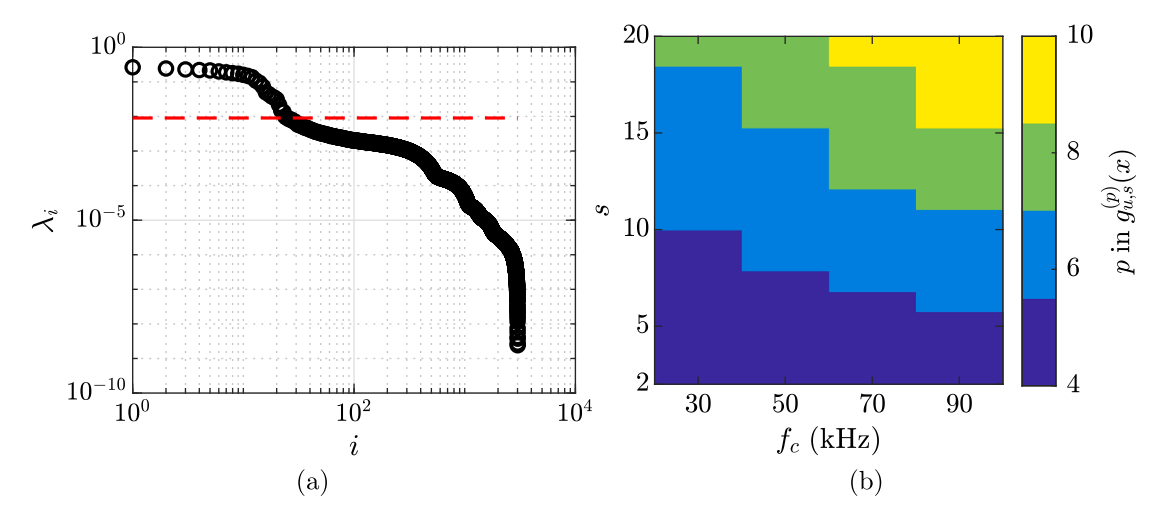


Fig. 10. (a) Singular values of the guided wavefield with $f_c = 30$ kHz and (b) p for suppressing $\hat{\phi}_t(x)$ for the four guided wavefields in the experimental validation. The empirical threshold for determining significant $\phi_t(x)$ is depicted by the horizontal dotted line in (a).

5. Concluding remarks

In this paper, a baseline-free structural damage identification method is developed for beam-like structures based on POMs of guided wavefields. The number of significant POMs is determined by an adaptive truncation technique, and it is shown local anomalies caused by the existence of damage exist in the significant POMs. Effects of global trends and noise of the significant POMs can be suppressed by the CWT with Gaussian wavelet functions of a proper order and scale parameters larger than a threshold scale parameter, respectively, and local anomalies of the significant POMs can be intensified by the CWT. The proper orders of Gaussian wavelet functions are successfully determined based on the modal assurance criterion and statistical criterion. The threshold scale parameter depends on noise levels, and its value can be obtained by observing damage identification results associated with different scale parameters. The effectiveness of the proposed method is investigated with different scenarios of damage and excitation forces. It was found that (1) the proposed method can accurately identify the location and extent of damage, and (2) the proposed method is robust for different scenarios of damage, excitation forces and measurement noise. In future works, it is worthwhile to conduct investigations on the location of damage at the end of beam-like structures by using POMs of guided wavefields.

CRediT authorship contribution statement

Wei Zhou: Conceptualization, Methodology, Software, Experimental test data acquiring, Writing – original draft. **Y.F. Xu:** Supervision, Conceptualization, Writing – review & editing, Funding acquisition.

Declaration of competing interest

The authors declare that they have no known competing financial interests or personal relationships that could have appeared to influence the work reported in this paper.

Data availability

Data will be made available on request.

Acknowledgments

The authors are grateful for the financial support from the National Science Foundation, USA through Grant No. CMMI-1762917. The authors gratefully acknowledge valuable experimental guidance from Jueseok Kim and some discussions with Dehong Fang.

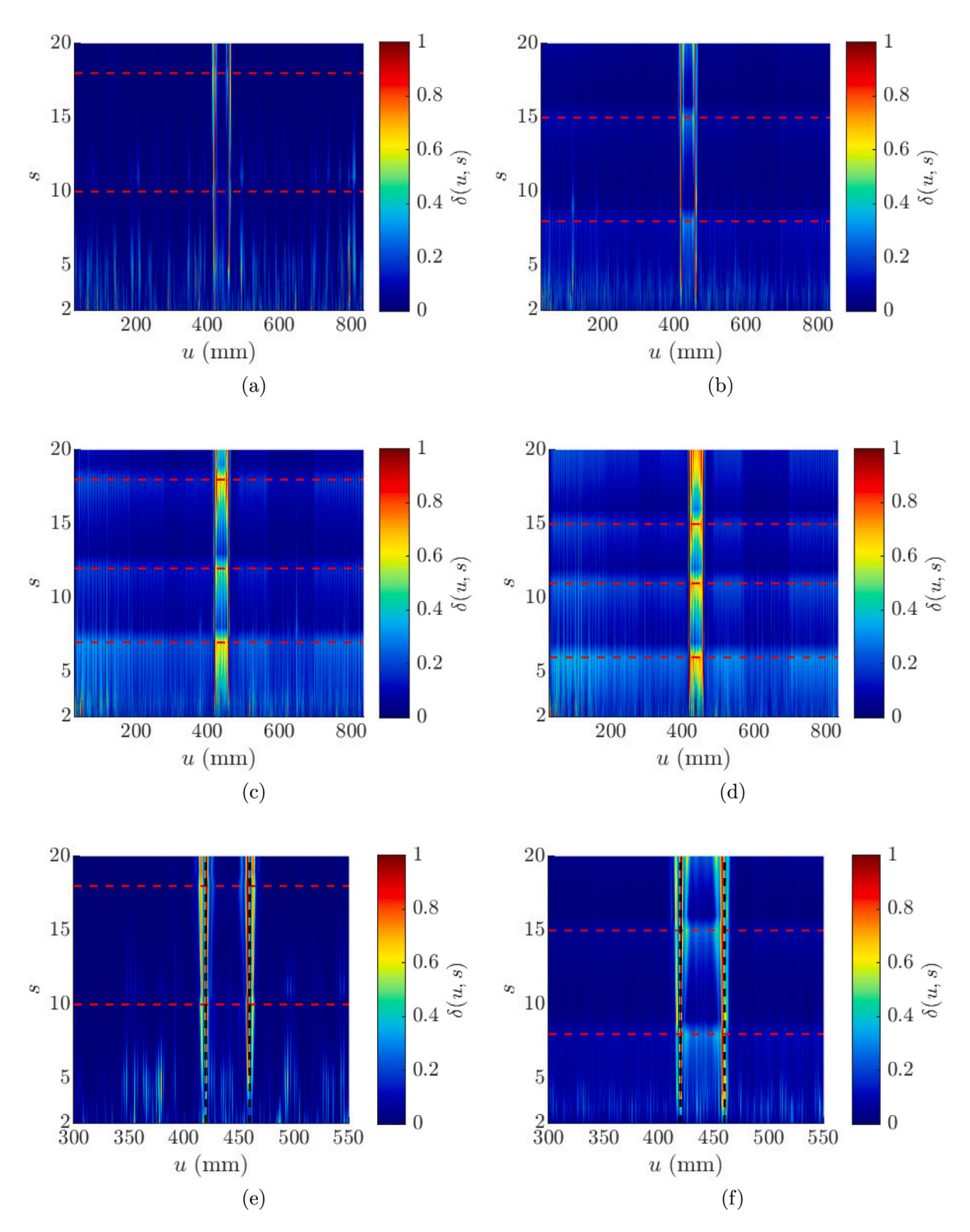


Fig. 11. Experimental damage identification results obtained from the guided wavefields with f_c being (a) 30 kHz, (b) 50 kHz, (c) 70 kHz, (d) 90 kHz, (e) a zoomed-in view of the damage area in (b). The boundaries of layers of values of p are depicted by the horizontal dotted lines. Edges of the damage area are depicted by two vertical dotted lines in (e) and (f).

References

- [1] M. Ruzzene, Frequency-wavenumber domain filtering for improved damage visualization, in: Ultrasonic and Advanced Methods for Nondestructive Testing and Material Characterization, World Scientific, 2007, pp. 591–611.
- [2] M. Ruzzene, S. Jeong, T. Michaels, J. Michaels, B. Mi, Simulation and measurement of ultrasonic waves in elastic plates using laser vibrometry, in: AIP Conference Proceedings, Vol. 760, American Institute of Physics, 2005, pp. 172–179.
- [3] L. Mallet, B. Lee, W. Staszewski, F. Scarpa, Structural health monitoring using scanning laser vibrometry: II. Lamb waves for damage detection, Smart Mater. Struct. 13 (2) (2004) 261.
- [4] Z.M. Master, T.E. Michaels, J.E. Michaels, Incident wave removal for defect enhancement in acoustic wavefield imaging, in: AIP Conference Proceedings, Vol. 894, 894, American Institute of Physics, 2007, pp. 665–672.
- [5] P. Kudela, M. Radzieński, W. Ostachowicz, Identification of cracks in thin-walled structures by means of wavenumber filtering, Mech. Syst. Signal Process. 50 (2015) 456–466.
- [6] G. Sha, H. Xu, M. Radzieński, M. Cao, W. Ostachowicz, Z. Su, Guided wavefield curvature imaging of invisible damage in composite structures, Mech. Syst. Signal Process. 150 (2021) 107240.
- [7] R. Basri, W. Chiu, Numerical analysis on the interaction of guided lamb waves with a local elastic stiffness reduction in quasi-isotropic composite plate structures, Compos. Struct. 66 (1–4) (2004) 87–99.
- [8] T.E. Michaels, J.E. Michaels, M. Ruzzene, Frequency-wavenumber domain analysis of guided wavefields, Ultrasonics 51 (4) (2011) 452-466.
- [9] M.D. Rogge, C.A. Leckey, Characterization of impact damage in composite laminates using guided wavefield imaging and local wavenumber domain analysis, Ultrasonics 53 (7) (2013) 1217–1226.
- [10] E.B. Flynn, S.Y. Chong, G.J. Jarmer, J.-R. Lee, Structural imaging through local wavenumber estimation of guided waves, NDT & E Int. 59 (2013) 1-10.
- [11] L. Yu, Z. Tian, Lamb wave structural health monitoring using a hybrid PZT-laser vibrometer approach, Struct. Health Monit. 12 (5-6) (2013) 469-483.
- [12] G. Kerschen, J.-c. Golinval, A.F. Vakakis, L.A. Bergman, The method of proper orthogonal decomposition for dynamical characterization and order reduction of mechanical systems: an overview, Nonlinear Dynam. 41 (1) (2005) 147–169.
- [13] C. Shane, R. Jha, Proper orthogonal decomposition based algorithm for detecting damage location and severity in composite beams, Mech. Syst. Signal Process. 25 (3) (2011) 1062–1072.
- [14] U. Galvanetto, G. Violaris, Numerical investigation of a new damage detection method based on proper orthogonal decomposition, Mech. Syst. Signal Process. 21 (3) (2007) 1346–1361.
- [15] U. Galvanetto, C. Surace, A. Tassotti, Structural damage detection based on proper orthogonal decomposition: experimental verification, AIAA J. 46 (7) (2008) 1624–1630.
- [16] E.-T. Lee, H.-C. Eun, Damage identification based on the proper orthogonal mode energy curvature, J. Vib. Acoust. 137 (4) (2015).
- [17] T. Teimoori, M. Mahmoudi, Damage detection in connections of steel moment resisting frames using proper orthogonal decomposition and wavelet transform, Measurement 166 (2020) 108188.
- [18] A. Chatterjee, An introduction to the proper orthogonal decomposition, Current Sci. (2000) 808-817.
- [19] Y. Xu, W. Zhu, J. Liu, Y. Shao, Identification of embedded horizontal cracks in beams using measured mode shapes, J. Sound Vib. 333 (23) (2014) 6273-6294
- [20] J.-P. Antoine, R. Murenzi, P. Vandergheynst, S.T. Ali, Two-Dimensional Wavelets and Their Relatives, Cambridge University Press, 2008.
- [21] S. Mallat, W.L. Hwang, Singularity detection and processing with wavelets, IEEE Trans. Inform. Theory 38 (2) (1992) 617-643.
- [22] M. Boltežar, J. Slavič, Enhancements to the continuous wavelet transform for damping identifications on short signals, Mech. Syst. Signal Process. 18 (5) (2004) 1065–1076.
- [23] S. Cao, H. Ouyang, Robust multi-damage localisation using common eigenvector analysis and covariance matrix changes, Mech. Syst. Signal Process. 111 (2018) 663–677.
- [24] S. Cao, H. Ouyang, L. Cheng, Baseline-free multidamage identification in plate-like structures by using multiscale approach and low-rank modelling, Struct. Control Health Monit. 26 (2) (2019) e2293.
- [25] W. Liu, W. Lin, Additive white Gaussian noise level estimation in SVD domain for images, IEEE Trans. Image Process. 22 (3) (2012) 872-883.
- [26] W. Zhou, Y. Xu, J. Kim, Baseline-free structural damage identification for plate-like structures based on two-dimensional curvature propagating flexural waves. J. Sound Vib. (2022) 117098.
- [27] R.J. Allemang, The modal assurance criterion-twenty years of use and abuse, Sound Vib. 37 (8) (2003) 14-23.
- [28] R.E. Walpole, Probability & Statistics for Engineers & Scientists, Prentice Hall, 2006.
- [29] S. Mallat, A Wavelet Tour of Signal Processing, Elsevier, 1999.